Karakoç, Alp; Paltakari, Jouni; Taciroglu, Ertugrul

On the computational homogenization of three-dimensional fibrous materials

Published in:
Composite Structures

DOI:
10.1016/j.compstruct.2020.112151

Published: 15/06/2020

Document Version
Peer-reviewed accepted author manuscript, also known as Final accepted manuscript or Post-print

Please cite the original version:
Karakoç, A., Paltakari, J., & Taciroglu, E. (2020). On the computational homogenization of three-dimensional fibrous materials. *Composite Structures*, *242*, Article 112151. https://doi.org/10.1016/j.compstruct.2020.112151

ON THE COMPUTATIONAL HOMOGENIZATION OF THREE-DIMENSIONAL FIBROUS MATERIALS

Alp Karakoç*,[1], Jouni Paltakari[1], Ertugrul Taciroglu[2]

[1]Aalto University, Department of Bioproducts and Biosystems, FI-00076 AALTO, FINLAND
[2]Civil and Environmental Engineering, University of California Los Angeles, 90095, CA, USA

ABSTRACT

Fibrous materials such as paper, nonwovens, textiles, nanocellulose based-biomaterials, polymer networks and composites are widely used versatile engineering materials. Deformations at the fiber network scale have direct role in their effective mechanical behavior. However, computational description of the deformations is a challenge due to their stochastic characteristics. In consideration to this issue, the current study presents a computational homogenization framework at the fiber network scale to investigate how the fiber properties affect the mechanical properties at material scale. Methodology is based on (I) geometrical, spatial and mechanical modelling of fibers and fiber-to-fiber interactions, (II) formation of fiber network solution domain, boundary nodes on the solution domain and control nodes of the domain bounding the solution domain. The boundary value problem is then defined at the fiber network scale and solved with the proposed framework using the Euclidean bipartite matching coupling the boundary nodes and the control nodes represented in the form of corner, edge and surface nodes. The computed results show that the framework is good at capturing the fibrous material characteristics at different scales and applicable to the solution domains generated with stochastic modelling or image-reconstruction methods resulting in non-conformal meshes with non-matching boundary node distributions.

Keywords: fibrous materials, nonwoven, nanocellulose, polymer network, computational homogenization, Euclidean bipartite matching.

* Corresponding author: alp.karakoc@alumni.aalto.fi (Alp Karakoç).

1. INTRODUCTION

Fibrous materials are versatile engineering materials that are used in a wide range of consumer and industrial products. These materials have notable properties for their mass production capabilities, lightweight, porous structure, high specific area and thermal properties. As illustrated in Figure 1, nonwoven fabrics, fiber mats and filters, sintered metallic fibers used as biomedical fabrics, hygiene products, apparel, filtration and insulation materials; felted or layered wood fibers used in paper and packaging products; and nanocellulose fibers used in regenerative medicine are prevalent examples of fibrous materials [1-5]. Mechanical characteristics of these materials are principally dependent on the mechanical, morphological and spatial parameters of the constituent fibers and their interactions—i.e. inter-fiber bonds [6, 7]. In order to investigate these parameters and provide the effective mechanical properties (of the material in focus) for deformation and manufacturing process simulations, bridging three different scales, which are fiber, fiber network and material scales, plays a crucial role [8-10]. It is noteworthy that the fiber network scale, in which the natural or artificial fibers are randomly or directionally aligned and bonded together through a chemical, mechanical and/or thermal process, form the main structural and physical foundations between the fiber and material scales.

In the literature, various fiber network models in two- and three-dimensional space have been provided [11-14]. Due to lower computational costs, two-dimensional models in the transverse plane, for which the networks are generated by the sequential random deposition of fibers connected together at their intersections, have been used to determine the in-plane mechanical behavior of specimens with thickness of order of one tenth or less of average fiber length [6, 15-17]. By means of these models, it is possible to directly compute the in-plane mechanical properties for the entire solution domain, which is computationally expensive; or to solve the boundary value problem (BVP) on the representative volume element (RVE), which is usually in the form of repetitive structural units representing the subscales of the material, resulting in the effective mechanical properties [18-20].

With increasing computational power, three-dimensional models, for which the fibers are deposited and bend on top of each other, have been of interest to determine the three-dimensional characteristics [3, 7, 21, 22]. In addition to mimicking the in-situ fiber network structures, the three-dimensional models also provide better insight into fiber and fiber network scale properties. Similar to the computational homogenization techniques in two-dimensional models, RVE is often modelled as a repeating unit, on the boundaries of which the periodic boundary conditions are defined [23, 24]. For repeating units, mesh conformality of the RVE boundary domain is essential—i.e. the boundary nodes on the opposing surfaces, edges and vertices should match. Besides, the choice and application of boundary conditions in heterogeneous materials, especially in case of fibrous materials, affect the results [25].

Therefore, in order to investigate the RVE response and solve the BVP for inherently non-conformal mesh—e.g. in case of reconstructed structural fiber network domain from image scanning tools or virtually generated domain based on statistical distributions— the present study proposes a three-dimensional fiber network modelling approach in the framework of computational homogenization. The main objective is to analyze how the fiber orientation distribution and fiber volume fraction affect the effective mechanical properties of fibrous materials. The boundary value problem (BVP) is thus defined at the fiber network scale, where the fiber network is taken to be the representative volume element (RVE) for the fibrous material. As a contribution to the previous computational efforts for such material systems, the boundary nodes of the RVE are linked to the control nodes of the domain bounding the RVE and BVP is solved on this domain instead of the RVE boundary domain, which is schematized in Figure 2 (and illustrated as Supplementary Materials). Here, the linking is achieved with the Euclidean bipartite matching technique aiming at minimizing the total distance between the control and boundary node sets. The boundary nodes are then kinematically coupled with the control nodes. Thereafter, periodic boundary conditions are enforced on the control nodes, rigid body rotations are eliminated and the BVP is solved in the computational homogenization framework based on the first order strain driven homogenization [26, 27]. The proposed solution technique is capable of bridging the scale-based features of both statistically defined and image-reconstructed domains—e.g. through laser scanning confocal microscopy, micro-computed tomography (μCT), scanning electron microscopy (SEM), magnetic resonance imaging (MRI) to name a few—for which non-conformal mesh exists and the same nodal distribution on the opposing boundaries does not hold [28, 29]. In addition to the proposed solution technique, a geometry transfer algorithm written as Python script is also provided, which is used to transfer the fiber geometry data directly from the technical computing software such as Mathematica, Matlab to the finite element analysis software—e.g. Abaqus. Therefore, it is possible to create and manipulate the mesh features and define finite element type and order by the pre-processing functionalities of the analysis software. This eliminates the difficult-to-handle data transferring through orphan mesh, with which fibers lack original geometry data created in the technical computing software.

2. METHODOLOGY

The present model follows three steps: (I) fiber formation by means of its geometrical, mechanical and spatial characteristics, (II) search for fiber intersections and fiber interaction assignments—i.e. bonding properties—, (III) formation and computational homogenization of the fiber network in order to bridge the fiber and material scale properties.

2.1. Fiber network generation

The geometrical model is designed for fibrous materials, the functionalities of which include the geometrical descriptions and labeling of individual fibers, their planar projections, fiber trimming and intersection search and labeling processes. A brief description of the model is given below (for more detailed information please see the authors' previous article [1]).

In *XYZ*-Cartesian coordinate system, each individual fiber is described in terms of its spatial properties—i.e. centroid $C(X_i, Y_i, Z_i)$ and $i \in \mathbb{Z}^+$, Azimuthal (in-plane) orientation θ and polar fiber orientation φ, and geometry—i.e. length l and cross-sectional properties including width w, height h, and wall thickness t. In addition to this, specimen is described as a rectangular prism with length L, width W and thickness T, which is composed of layers with thickness T_{layer} as seen in Figure 3.

In order to define the spatial distribution of fibers, fiber centroids are first uniformly distributed. For avoiding the use of same fiber centroids and randomness in centroid picking, Monte Carlo simulation are carried out in an iterative manner. Thereafter, as depicted in the flowchart of Figure 4, the fiber deposition process is carried out as a function of the abovementioned spatial and geometric parameters for each layer till the predetermined fiber volume fraction $V_f = \sum_{f=1}^{n} v_f \Big/ V$,

which is the ratio between the total fiber volume $\sum_{f=1}^{n} v_f$ and the specimen volume $V = L \times W \times T$, is satisfied.

During each deposition, intersection search process—i.e. contact detection—, is also implemented to find the adjacent fibers with the nearest neighboring algorithm provided previously by the authors [1]. The intersection process is essential in reforming the fibers, determination of the fibers in contact and solving the contact problem as shown in Figure 5.

2.2. Computational homogenization framework

The generated geometrical model is meshed with C3D8R 8-node hexahedral solid element with reduced integration by means of the built-in meshing capability of commercial finite element solver Abaqus [30]. For this purpose, Python scripting interface for Abaqus is implemented. First, all the fibers are created as part objects and then assigned as assembly instances using the translation and rotation functions, for which a sample script can be found in the Appendix. Here, the fibers are taken to be linear elastic with orthotropic material behavior while fiber intersections are assumed to be perfectly bonded, the intersection regions of which are illustrated in Figure 5. Abaqus/Explicit, which uses explicit time integration method calculating the nodal accelerations at every time step, is thereafter used to solve the problem.

As schematically illustrated in Figure 2, in order to solve the BVP at the representative volume element RVE scale, the boundary nodes p on the RVE boundaries $\partial\omega$ are first determined. Here, it is noteworthy that boundary nodes p are traced and stored during the network formation process, or can be also extracted—e.g. with Tetgen libraries—in case of using orphan mesh [31]. The boundary nodes p are thereafter matched with the control nodes q, which are discretized and represented in the form of corner, edge, and surface nodes on the boundaries of the domain $\partial\Gamma$ bounding RVE. The matching is achieved through the Euclidean bipartite matching, for which $n \times n$ distance matrix

$$\begin{bmatrix} \mathbf{d}(p_1,q_1) & \mathbf{d}(p_1,q_2) & \dots & \mathbf{d}(p_1,q_n) \\ \mathbf{d}(p_2,q_1) & \dots & \dots & \dots \\ \dots & \dots & \dots & \dots \\ \mathbf{d}(p_n,q_1) & \dots & \dots & \mathbf{d}(p_n,q_n) \end{bmatrix} \tag{1}$$

is generated based on the Euclidean distance **d** of each (p, q) combination with n being the set length of p (or q). Then, the optimal permutation of matched nodes is discerned based on their total Euclidean distance T through the minimization problem [32, 33]

$$T = \min \sum_{\Pi} \mathbf{d}(p,q) \tag{2}$$

where $\prod$ is the permutations that abide a one-to-one correspondence as depicted in Figure 2(b) (Link and couple). The problem expressed in Eq. (2) is solved with Kuhn–Munkres algorithm, details of which can be found in [34, 35]. As shown in Figure 2(a) (Match), after minimization and one-to-one matching, boundary nodes p are constrained to follow the degrees of freedom of the control nodes q (i.e. $\vec{u}_p = \vec{u}_q$), which allows to define the RVE boundary conditions over $\partial\Gamma$ as a conformal boundary domain. Periodic boundary conditions are thereafter applied on $\partial\Gamma$, rigid body rotations are eliminated, and the BVP is solved.

In consideration to the convergence towards effective material properties, periodic boundary conditions are imposed over $\partial\Gamma$ in the first-order strain driven homogenization. As depicted in Figure 6, the macro-strain $\mathbf{e}^{\mathrm{M}}$ is known *a priori* where the associated macro-stress $\mathbf{s}^{\mathrm{M}}$ is computed through volume averaging of the stress field at the RVE scale [36].

Here, the macro-strain e_{ij}^{M} for $i, j \in \{X, Y, Z\}$ is the given parameter and is used as the driving parameter of the microscopic displacement field for the RVE so that

$$\vec{u}^{\mathrm{m}} = \vec{r} \cdot \mathbf{e}^{\mathrm{M}} + \underline{\vec{u}}. \tag{3}$$

The first addend of Eq. (3) on the right-hand side represents the macroscopic displacement contribution, and the second represents the displacement fluctuation field $\underline{\vec{u}}$ due to heterogeneities within the RVE [26]. Here, $\vec{r}$ represents the position vector between two nodes and the overall body is assumed to be composed of repeating rectangular prism bounding the RVEs. Continuity conditions for the displacement field are satisfied at each adjacent boundary by taking the relative positions of the control node sets q, which eliminates $\underline{\vec{u}}$.

In computational homogenization studies, the use of RVEs with periodic boundary conditions is a common practice, for which the corresponding corner, edge and surface nodes are matched as depicted in Figure 7, and suffices to represent the effective material deformation [27]. Following this common practice, periodic boundary conditions are applied onto the control nodes q of the domain $\partial\Gamma$ bounding the RVE. Here, it is important that the so-called "periodic offset" caused by the distance between matched nodes is inevitable.

In computational homogenization, Hill-Mandel principle gives the relationship between the micro- and material scales such that

$$\mathbf{s}^{\mathrm{M}} : \mathbf{e}^{\mathrm{M}} = \frac{1}{\Gamma}\int_{\Gamma} \mathbf{s}^{\mathrm{m}} : \mathbf{e}^{\mathrm{m}} \,\mathrm{d}\Gamma \,, \tag{4}$$

for which superscripts m and M stand for micro- and material scales. The symbol (:) denotes the inner product $\mathbf{a} : \mathbf{b} = a_{ij} b_{ij}$ for second-order tensors. By using the Gauss theorem, Eq. (4) can be rewritten over the $\partial\Gamma$ as

$$\mathbf{s}^{\mathrm{M}} : \mathbf{e}^{\mathrm{M}} = \frac{1}{\Gamma}\int_{\partial\Gamma} \vec{t}^{\,\mathrm{m}} \cdot \vec{u}^{\,\mathrm{m}} \,\mathrm{d}\partial\Gamma \,, \tag{5}$$

where $\vec{t}^{\,\mathrm{m}}$ is the micro-scale traction vector at $\partial\Gamma$. By plugging the boundary periodicity into Eq. (5),

$$\mathbf{s}^{\mathrm{M}} : \mathbf{e}^{\mathrm{M}} = \frac{1}{\Gamma}\int_{\partial\Gamma} \vec{t}^{\,\mathrm{m}} \cdot \left(\vec{r} \cdot \mathbf{e}^{\mathrm{M}}\right) \mathrm{d}\partial\Gamma + \frac{1}{\Gamma}\int_{\partial\Gamma} \vec{t}^{\,\mathrm{m}} \cdot \underline{\vec{u}} \,\mathrm{d}\partial\Gamma, \tag{6}$$

which can be rearranged into

$$\mathbf{s}^{\mathrm{M}} : \mathbf{e}^{\mathrm{M}} = \frac{1}{\Gamma}\int_{\partial\Gamma} \left(\vec{t}^{\,\mathrm{m}} \otimes \vec{r}\right) \mathrm{d}\partial\Gamma : \mathbf{e}^{\mathrm{M}} + \frac{1}{\Gamma}\int_{\partial\Gamma} \vec{t}^{\,\mathrm{m}} \cdot \underline{\vec{u}} \,\mathrm{d}\partial\Gamma \,. \tag{7}$$

Here, the symbol $\otimes$ denotes the dyadic operator. The second integrand at the right-hand side vanishes in case of periodic boundary conditions. Hence, macro-scale stress $\mathbf{s}^{\mathrm{M}}$ can be expressed as the volume average of the micro-scale stress $\mathbf{s}^{\mathrm{m}}$ such that

$$\mathbf{s}^{\mathrm{M}} = \frac{1}{\Gamma} \int_{\partial\Gamma} \left(\vec{t}^{\,\mathrm{m}} \otimes \vec{r} \right) \mathrm{d}\partial\Gamma = \frac{1}{\Gamma} \int_{\Gamma} \mathbf{s}^{\mathrm{m}} \, \mathrm{d}\Gamma, \tag{8}$$

where Γ is the volume of the rectangular prism bounding the RVE. Then, the given strains $\mathbf{e}^{\mathrm{M}}$ and the computed stresses $\mathbf{s}^{\mathrm{M}}$ at the material scale can be combined. Eventually, by means of the least-squares minimization of six distinct deformation modes in three-dimensional space (three axial tension $\mathbf{e}^{\mathrm{M}}_{XX}, \mathbf{e}^{\mathrm{M}}_{YY}, \mathbf{e}^{\mathrm{M}}_{ZZ}$ and three shear $\mathbf{e}^{\mathrm{M}}_{XY}, \mathbf{e}^{\mathrm{M}}_{YZ}, \mathbf{e}^{\mathrm{M}}_{ZX}$ loading modes), the compliance $\mathbf{C}^{\mathrm{M}}$ is obtained as

$$\mathcal{C}(C_{11},..,C_{66}) = \sum_{i=1}^{n} \left\| \mathbf{e}^{\mathrm{M}}_{i} - \mathbf{C}^{\mathrm{M}} : \mathbf{s}^{\mathrm{M}}_{i} \right\|^{2}, \tag{9}$$

where i refers to the number of experiments [37, 38]. Under the assumption of material orthotropy, $\mathbf{C}^{\mathrm{M}}$ for three-dimensional case is expressed as

$$\left[\mathbf{C}^{\mathrm{M}}\right] = \begin{bmatrix} 1/E_X & -\nu_{YX}/E_Y & -\nu_{ZX}/E_Z & 0 & 0 & 0 \\ -\nu_{XY}/E_X & 1/E_Y & -\nu_{ZY}/E_Z & 0 & 0 & 0 \\ -\nu_{XZ}/E_X & -\nu_{YZ}/E_Y & 1/E_Z & 0 & 0 & 0 \\ 0 & 0 & 0 & 1/G_{YZ} & 0 & 0 \\ 0 & 0 & 0 & 0 & 1/G_{ZX} & 0 \\ 0 & 0 & 0 & 0 & 0 & 1/G_{XY} \end{bmatrix}, \tag{10}$$

for which E_X, E_Y, E_Z are the elastic moduli, G_{YZ}, G_{ZX}, G_{XY} are the shear moduli and $\nu_{XY}, \nu_{YX}, \nu_{XZ}, \nu_{ZX}, \nu_{YZ}, \nu_{ZY}$ are the Poisson's ratios defined in the global (specimen) *XYZ*-Cartesian coordinate system (please, see Figure 3(b)). Here, it is also noteworthy that $\mathbf{C}^{\mathrm{M}}$ is computed under the assumption of small strains, for which the fiber bending is dominant mode resulting in non-affine deformations [13].

3. RESULTS AND DISCUSSIONS

3.1. Design of experiments and representative volume element (RVE) size

As previously described, fibers in the present investigations were selected to be linear elastic with orthotropic material properties. Due to complexities in three-dimensional characterization of single fiber measurements, the literature values for wood fibers were adapted as E_x=15000 MPa, E_y=E_z=5000 MPa, G_{xy}=G_{xz}=3000 MPa, G_{yz}=1080 MPa, v_{xy}=v_{xz}=0.066, v_{yz}=0.39, for which the subscripts x, y and z refer to the axes of the local (fiber) xyz-Cartesian coordinate system (please, see Figure 3(a)) [39-42]. Fibers were assumed to be fully bonded and deformed under maximum macro-strain value of $\max\left(e_{ij}^{\mathrm{M}}\right)=0.025$ to understand the effects of the Azimuthal orientation variation $\Delta\theta$ and the volume fraction of fibers V_f. For these investigations, the constant fiber parameters were fiber length l=1.5 mm, width w=0.025 mm, height h=0.010 mm, wall thickness t=0.004 mm, specimen layer thickness was T_{layer}=0.020 mm, and polar orientation was taken to be φ=0° because of the formation characteristics following the values from the literature [43].

As listed in Table 1, three different RVE sets (Sets 1-3), which are $L\times W\times T$ = 2×2×0.006 mm^3, $L\times W\times T$ = 3×3×0.006 mm^3 and $L\times W\times T$ = 4×4×0.006 mm^3 with $\Delta\theta$=±90° and $V_f\approx$0.20, were initially studied to determine the computationally effective RVE size to be used for the parametric investigations. Thereafter, in order to study the effects of $\Delta\theta$ and V_f on the number of fiber crossings per fiber and the effective elastic properties of the fibrous material, simulation experiments were carried out for each set (Sets 4-6 for $\Delta\theta$ and Sets 7-10 for V_f as tabulated in Table 1). Due to individual fiber properties being assigned various values in the literature, the computed effective elastic properties were normalized with respect to E_x for the comparative analyses. So as to create two parameter statistical description (μ - mean value, σ - standard deviation), all the simulation sets were repeated three times. Due to large number of degrees of freedom in each simulation, parallel computations were carried out on CSC - IT Center for Science Taito (Finland) supercluster, through which Xeon E5-2680 v3 CPUs with 12 cores each running at 2.5GHz and 64 GB RAM memory were allocated.

The normalized effective elastic properties listed in Table 2 indicate that the RVE solution domain size for the selected ranges has negligible effects. Taken this outcome and computational efficiency into account, the solution domain size was set to $L \times W \times T$ = 2×2×0.006 mm^3 for the simulations regarding the effects of $\Delta\theta$ and V_f.

3.2. Fiber orientation distribution and volume fraction

The fiber orientation distribution and volume fraction are principally inherited from the fiber deposition during the manufacturing process. For instance, the fiber alignment distribution in the machine and cross directions in case of paper formation is a scrutinized phenomenon, which provides the material orthotropic characteristics [44]. In consideration to this effect, three different Azimuthal orientation variation configurations $\Delta\theta$ = {±15°, ±45°, ±90°} were investigated, for which the Azimuthal orientation was taken to be θ=0°. Some of these configurations are depicted in Figure 8 for a better visual understanding.

Here, it is also noteworthy that continuous probability distribution $\underline{P}$, which is expressed in terms of log-normal distribution due to positive and non-symmetric simulation results, was applied to investigate the effects of fiber parameters on the number of crossings per fiber n_{cpf} as follows

$$\underline{P}(n_{\mathrm{cpf}}, \zeta) = \frac{\exp\left(-\dfrac{\left(-\mu_{\mathrm{d}}(\zeta) + \ln(n_{\mathrm{cpf}})\right)^2}{2\left(\sigma_{\mathrm{d}}(\zeta)\right)^2} \right)}{\sqrt{2\pi}\, n_{\mathrm{cpf}}\, \sigma_{\mathrm{d}}(\zeta)}. \tag{11}$$

Here, π is the Pi number, exp refers to the exponential function, ln is the natural logarithm while μ_{d} and σ_{d} are the mean and standard deviation of the continuous probability distribution, which are first order (linear) polynomial functions of the tested parameter—e.g. $\Delta\theta$, V_f in the present study— and represented with variable ζ taking the form $\mu_{\mathrm{d}}(\zeta)$ and $\sigma_{\mathrm{d}}(\zeta)$. Hence, it was possible to fit the simulation results by means of Eq. (11) and estimate the distribution for the investigated parameters.

As seen in Figure 8 and Table 3, the probability distribution functions $\underline{P}(n_{\mathrm{cpf}}, \Delta\theta)$ indicate that the increase in $\Delta\theta$ results in more randomly oriented fibers. As a result of this, fibers build up more crossings per fiber, thus increasing n_{cpf}. Besides, increase in $\Delta\theta$ leads to a more even $\underline{P}(n_{\mathrm{cpf}}, \Delta\theta)$ with lower peak percentages. Due to this increase, random directional properties are more emphasized, which results in a trend between the transverse (in-plane) isotropy and $\Delta\theta$—e.g, highly directional material properties with $\mu(E_X/E_x)$= 0.281 and $\mu(E_Y/E_x)$= 0.065 for $\Delta\theta$= ±15 and isotropic properties with $\mu(E_X/E_x)$= 0.256 and $\mu(E_Y/E_x)$= 0.256 for $\Delta\theta$= ±90. In addition to this trend, there is an increase in G_{YZ} and ν_{XZ} with $\Delta\theta$ while G_{XZ} and ν_{YZ} decrease with $\Delta\theta$. However, there is a remittent relationship between G_{XY}, ν_{XY} and $\Delta\theta$. The reason for these fluctuations is mainly due to the combined effects of $\Delta\theta$ and V_f variations. In addition, the effect of $\Delta\theta$ on E_Z seems to be negligible showing the minimal contribution of $\Delta\theta$ on the out of plane deformation characteristics.

Following the $\Delta\theta$ investigations, fiber volume fraction V_f effects were analyzed for different configurations $V_f \approx\{0.18, 0.25, 0.27, 0.30\}$ where $\Delta\theta$ was taken as ±90° for all the cases as represented in Table 1. The normalized results listed in Table 4 show that V_f has incontrovertible influence on the effective in-plane elastic moduli E_X, E_Y and all three shear moduli G_{XY}, G_{XZ}, G_{YZ}. This is also evident through the increase in n_{cpf} shown in Figure 9. It is also noteworthy that the variations in $\underline{P}(n_{\mathrm{cpf}}, V_f)$ are reduced with V_f. This shows the fibers are more entangled and forming more bonding—e.g. max(n_{cpf})=90 for V_f≈0.18 while max(n_{cpf})=124 for V_{f}≈0.30 — with uniform distribution, which contributes to the stiffness in the material scale. However, similar to the $\Delta\theta$ investigations, there is no clear influence of V_f on E_Z. This may imply that the axial tensile loading along Z-axis is insensitive to the increase in V_f—i.e., the densification of the fiber network.

4. CONCLUSIONS

In the present study, a computational homogenization framework at the fiber network scale was provided to investigate the influence of fiber scale parameters on the effective mechanical properties at the material scale. The methodology was initiated with geometrical and mechanical formation of individual fibers and fiber-to-fiber interactions, which formed the fiber network solution domain. Thereafter, the domains were used as RVEs and BVPs were solved over the RVE boundaries by means of the detailed framework. For the BVPs, three axial tension $\mathbf{e}^{\mathrm{M}}_{XX}, \mathbf{e}^{\mathrm{M}}_{YY}, \mathbf{e}^{\mathrm{M}}_{ZZ}$

and three shear $\mathbf{e}_{XY}^{\mathrm{M}}, \mathbf{e}_{YZ}^{\mathrm{M}}, \mathbf{e}_{ZX}^{\mathrm{M}}$ loading modes were used to obtain the compliance $\mathbf{C}^{\mathrm{M}}$. The case studies indicated the influence of Azimuthal (in-plane) orientation distributions $\Delta\theta$ on the material isotropy while the increase in fiber volume fraction V_f contributes to the material stiffness. It was observed that both investigated parameters have close relationship with the number of crossing per fiber n_{cpf}.

The present framework is believed to advance the analyses of fiber scale geometrical, spatial and mechanical parameters on the effective mechanical characteristics at the material scale. Especially, it establishes a multiscale modelling platform for fibrous materials, the solution domains of which can be generated with stochastic modelling tools or image-reconstruction methods resulting in non-conformal meshes with non-matching nodal distributions on the RVE boundaries. Nevertheless, a computational homogenization framework investigating several length scales will be a complement to the introduced methodology. Further studies including cyclic and compressive loading modes, constitutive material models with hardening and rate-dependency, and fiber-to-fiber interaction with cohesive bonding models can be then evaluated for a complete package for process simulations and structural analyses.

ACKNOWLEDGMENTS

The authors wish to acknowledge CSC – IT Center for Science, Finland, for the computational resources.

REFERENCES

[1] Karakoc A, Hiltunen E, Paltakari J. Geometrical and spatial effects on fiber network connectivity. Composite Structures 2017; 168: 335-344.

[2] Kulachenko A, Uesaka T. Direct simulations of fiber network deformation and failure. Mech Mater 2012; 51(0): 1-14.

[3] Iorga L, Pan Y, Pelegri A. Numerical characterization of material elastic properties for random fiber composites. J Mech Mater Struct 2008; 3(7): 1279-1298.

[4] Karakoç A. A fiber network model to understand the effects of fiber length and height on the deformation of fibrous materials. Research on Engineering Structures and Materials 2016; 2(2): 51-57.

[5] Greca L, Lehtonen J, Tardy B, Rafiee M, Karakoç A, Mattos B, Rojas O. 3D bacterial cellulose biofabrication using superhydrophobized molds: Fundamentals and opportunities. Abstracts of papers of the American Chemical Society, 257.

[6] Sampson W. Modelling stochastic fibrous materials with Mathematica, London: Springer-Verlag, 2009.

[7] Lavrykov S, Lindström SB, Singh KM, Ramarao BV. 3D network simulations of paper structure. Nordic Pulp Paper Research Journal 2012; 27(2): 256-263.

[8] Targhagh M. Simulation of the mechanical behaviour of low-density paper and an individual inter-fibre bond. MSc. Thesis, Vancouver: University of British Columbia, 2016.

[9] Alava M, Niskanen K. The physics of paper. Reports on progress in physics 2006; 69: 669-723.

[10] Curto JMR, Conceição ELT, Portugal ATG, Simões RMS. Three-dimensional modelling of fibrous materials and experimental validation. Materialwissenschaft und Werkstofftechnik 2011; 42(5): 370-374.

[11] Provatas N, Haataja M, Asikainen J, Majaniemi S, Alava MJ, Nissila AT. Fiber deposition models in two and three spatial dimensions. Colloids and Surfaces A 2000; 165: 209-229.

[12] Bosco E, Peerlings R, Geers M. Asymptotic homogenization of hygro-thermo-mechanical properties of fibrous networks. International Journal of Solids and Structures 2017; 115–116: 180-189.

[13] Berkache K, Deogekar S, Goda I, Picu RC, Ganghoffer J-F. Identification of equivalent couple-stress continuum models for planar random fibrous media. Continuum Mechanics and Thermodynamics 2019; 31: 1035.

[14] Rahali Y, Assidi M, Goda I, Zghal A, Ganghoffer J-F. Computation of the effective mechanical properties including nonclassical moduli of 2.5 D and 3D interlocks by micromechanical approaches. Composites Part B: Engineering 2016; 98: 194-212.

[15] Kahkonen S. Elasticity and stiffness evolution in random fibre networks, Licentiate Thesis, Jyvaskyla: University of Jyvaskyla, 2003.

[16] Berkache K, Deogekar S, Goda, Picu RC, Ganghoffer J-F. Construction of second gradient continuum models for random fibrous networks and analysis of size effects. Composite Structures 2017; 181: 347-357.

[17] Berkache K, Deogekar S, Goda, Picu RC, Ganghoffer J-F. Homogenized elastic response of random fiber networks based on strain gradient continuum models. Mathematics and Mechanics of Solids 2019; 24: 3880-3896.

[18] Farukh F, Demirci E, Ali H, Acar M, Pourdeyhimi B, Silberschmidt V. Nonwovens modelling: a review of finite-element strategies. The Journal of The Textile Institute 2015; 4: 1-8.

[19] Bronkhorst CA. Modelling paper as a two-dimensional elastic-plastic stochastic network. International Journal of Solids and Structures 2003; 40: 5441-5454.

[20] Chen N, Silberstein M. A micromechanics-based damage model for non-woven fiber networks. International Journal of Solids and Structures 2019; 160: 18-31.

[21] Pan Y. Stiffness and progressive damage analysis on random chopped fiber composite using FEM. PhD Thesis, New Brunswick, New Jersey: Rutgers, The State University of New Jersey, 2010.

[22] Jin BC. 3-D numerical simulation and analysis of complex fiber geometry RaFC materials with high volume fraction and high aspect ratio based on Abaqus Python. PhD Thesis, New Brunswick, New Jersey: Rutgers, The State University of New Jersey, 2011.

[23] Persson J, Isaksson P. A mechanical particle model for analyzing rapid deformations and fracture in 3D fiber materials with ability to handle length effects. International Journal of Solids and Structures 2014; 51: 2244-2251.

[24] Li Y, Stapleton S, Reese S, Simon J. Anisotropic elastic-plastic deformation of paper: Out-of-plane model. International Journal of Solids and Structures 2018; 130: 172-182.

[25] Inglis H, Geubelle P, Matouš K. Boundary condition effects on multiscale analysis of damage localization. Philosophical Magazine 2008; 88(16): 2373-2397.

[26] Geers M, Kouznetsova V, Brekelmans W. Multi-scale computational homogenization: Trends and challenges. Journal of Computational and Applied Mathematics 2010; 234(7): 2175-2182.

[27] Karakoç A. Sensitivity analysis on the effective stiffness properties of 3-D orthotropic honeycomb cores. International Journal for Computational Methods in Engineering Science and Mechanics 2018; 19(1): 22-30.

[28] Nguyen V, Béchet E, Geuzaine C, Noels L. Imposing periodic boundary condition on arbitrary meshes by polynomial interpolation. Computational Materials Science 2012; 55: 390-406.

[29] Nguyen V, Noels L. Computational homogenization of cellular materials. International Journal of Solids and Structures 2014; 51(11-12): 2183-2203.

[30] Hibbitt, Karlsson and Sorensen, ABAQUS: Theory Manual, Providence, R.I.: Hibbitt, Karlsson & Sorensen, 1992.

[31] Si H. TetGen, A Delaunay-based quality tetrahedral mesh generator. ACM Trans. on Mathematical Software 2015; 41(2): 36 pages.

[32] Karakoc A, Taciroglu E. Optimal automated path planning for infinitesimal and real-sized particle assemblies. AIMS Materials Science 2017; 4(4): 847-855.

[33] Karakoc A, Keles O. A predictive failure framework for brittle porous materials via machine learning and geometric matching methods. Journal of Materials Science 2019, doi:10.1007/s10853-019-04339-1.

[34] Rendl F. On the Euclidean assignment problem. Journal of Computational and Applied Mathematics 1988; 23(3): 257-265.

[35] Hung M, Rom W. Solving the Assignment Problem by Relaxation. Operations Research 1980; 28(4): 969-982.

[36] Hernández J, Oliver J, Huespe A, Caicedo M, Cante JC. High-performance model reduction techniques in computational multiscale homogenization. Computer Methods in Applied Mechanics and Engineering 2014; 276: 149-189.

[37] Karakoç A, Tukiainen P, Freund J, Hughes M. Experiments on the effective compliance in the radial–tangential plane of Norway spruce. Composite Structures 2013; 102: 287-293.

[38] Sjolund J, Karakoç A, Freund J. Accuracy of regular wood cell structure model. Mechanics of Materials 2014; 76: 35-44.

[39] Neagu R, Gamstedt E, Lindström M. Influence of wood-fibre hygroexpansion on the dimensional instability of fibre mats and composites. Composites Part A: Applied Science and Manufacturing 2005; 36(6): 772-788.

[40] K. Persson. Micromechanical modelling of wood and fibre properties. PhD Thesis, Lund: Lund University, Department of Mechanics and Materials, 2000.

[41] Jäger A, Bader T, Hofstetter K, Eberhardsteiner J. The relation between indentation modulus, microfibril angle, and elastic properties of wood cell walls. Composites Part A: Applied Science and Manufacturing 2011; 42(6): 677-85.

[42] Sedighi-Gilani M, Navi P. Experimental observations and micromechanical modeling of successive-damaging phenomenon in wood cells' tensile behavior. Wood science and technology 2007; 41(1): 69-85.

[43] Niskanen K. Paper Physics 1998. Finland: Fapet Oy.

[44] Cox HL. The elasticity and strength of paper and other fibrous materials. British Jounal of Applied Physics 1952; 3: 72-79.

APPENDIX

An example Python script for direct data transfer to Abaqus finite element solver: Fiber part creation and assembly formation

```
from abaqus import*
from part import*
from material import*
from section import*
from assembly import*
from step import*
from interaction import*
from load import*
from mesh import *
from job import *
from sketch import *
from visualization import *
from connectorBehavior import *

#PART#
#FIBER CENTERLINE FORMATION#
mdb.models['Model'].ConstrainedSketch(name='__sweep__', sheetSize=1.0)
mdb.models['Model'].sketches['__sweep__'].Line(point1=(CX1, CY1),point2=(CX2, CY2))
mdb.models['Model'].sketches['__sweep__'].Line(point1=(CX2, CY2),point2=(CX3, CY3))
mdb.models['Model'].sketches['__sweep__'].Line(point1=(CX3, CY3),point2=(CX4, CY4))
…….
…….
mdb.models['Model'].ConstrainedSketch(name='__profile__', sheetSize=1.0, transform=(0.0,
0.0, 0.0, 0.0, 0.0, 0.0, 0.0, 0.0, 0.0, 0.0, 0.0, 0.0))

#FIBER OUTER BORDER FORMATION#
```

```
mdb.models['Model'].sketches['__profile__'].rectangle(point1=(OX1, OY1), point2=(OX2, OY2))

#FIBER HOLE BORDER FORMATION#
mdb.models['Model'].sketches['__profile__'].rectangle(point1=(HX1, HY1), point2=(HX2, HY2))
# PART FORMATION#
mdb.models['Model'].Part(dimensionality=THREE_D,name='Part-1', type=DEFORMABLE_BODY)
mdb.models['Model'].parts['Part-1'].BaseSolidSweep(path=mdb.models['Model'].sketches['__sweep__'],sketch=mdb.models['Model'].sketches['__profile__'])
del mdb.models['Model'].sketches['__profile__']
del mdb.models['Model'].sketches['__sweep__']

#ASSEMBLY#
#ASSEMBLY INSTANCE FORMATION#
#ONE SHOULD OBTAIN (1) TRANSLATION VECTOR, (2) PIVOT POINT FOR ROTATION—E.G. FIRST POINT OF FIBER CENTERLINE, (3) AZIMUTHAL (IN-PLANE) ORIENTATION ANGLE OF EACH FIBER FROM TECHNICAL COMPUTING SOFTWARE IN ADVANCE#

mdb.models['Model'].rootAssembly.DatumCsysByDefault(CARTESIAN)
mdb.models['Model'].rootAssembly.Instance(dependent=ON,name='Part-1-1',part=mdb.models['Model'].parts['Part-1'])
mdb.models['Model'].rootAssembly.rotate(angle=90.0,axisDirection=(1.0,0.0,0.0),axisPoint=(0.0,0.0,0.0),instanceList=('Part-1-1',))
mdb.models['Model'].rootAssembly.translate(instanceList=('Part-1-1',),vector=(TX, TY, TZ))
mdb.models['Model'].rootAssembly.rotate(angle=θZ,axisDirection=(0.0,0.0,1.0),axisPoint=(PX, PY, PZ), instanceList=('Part-1-1',))
```

List of Tables

Table 1: Design of experiments. The geometrical and spatial parameters are as follows: L, W, T are specimen length, width and thickness, respectively; $\Delta\theta$ is the Azimuthal orientation variation and V_f is the fiber volume fraction in the confined specimen space. Here, μ and σ refer to the mean value and standard deviation, respectively.

Description	Set	L (mm)	W (mm)	T (mm)	$\Delta\theta$ (º)	V_f (set) (-)	V_f (computed) (-) (μ, σ)	Number of fibers (-) (μ, σ)
RVE Size	1	2.0	2.0	0.006	±90	0.20	0.206, 0.004	276, 8
	2	3.0	3.0	0.006	±90	0.20	0.204, 0.004	541, 4
	3	4.0	4.0	0.006	±90	0.20	0.208, 0.001	937, 5
Azimuthal orientation variation $\Delta\theta$ (º)	4	2.0	2.0	0.006	±15	0.28	0.283, 0.011	344, 13
	5	2.0	2.0	0.006	±45	0.28	0.281, 0.007	372, 13
	6	2.0	2.0	0.006	±90	0.28	0.273, 0.005	367, 12
Volume Fraction V_f (-)	7	2.0	2.0	0.006	±90	0.18	0.182, 0.001	245, 3
	8	2.0	2.0	0.006	±90	0.25	0.249, 0.003	303, 2
	9	2.0	2.0	0.006	±90	0.27	0.273, 0.005	367, 12
	10	2.0	2.0	0.006	±90	0.30	0.304, 0.004	402, 5

Table 2: RVE size and normalized effective elastic properties. Here, μ and σ are the mean value and standard deviation, respectively. Approximate CPU times for the simulations are based on the Xeon E5-2680 v3 CPUs with 12 cores each running at 2.5GHz and 64 GB RAM memory configuration. Here, Azimuthal orientation variation and volume fractions are taken as $\Delta\theta$=±90° and V_f≈0.20, respectively.

Set	$\frac{E_X}{E_x}$ (-) (μ, σ)	$\frac{E_Y}{E_x}$ (-) (μ, σ)	$\frac{E_Z}{E_x}$ (-) (μ, σ)	$\frac{G_{XY}}{E_x}$ (-) (μ, σ)	$\frac{G_{XZ}}{E_x}$ (-) (μ, σ)	$\frac{G_{YZ}}{E_x}$ (-) (μ, σ)	ν_{XY} (-) (μ, σ)	ν_{XZ} (-) (μ, σ)	ν_{YZ} (-) (μ, σ)	CPU time (sec)
1 (L=2 mm, W=2 mm)	0.196	0.198	0.043	0.045	0.014	0.014	0.096	0.095	0.019	~ 5400
	0.006	0.003	0.002	0.001	0.001	0.000	0.003	0.005	0.002	
2 (L=3 mm, W=3 mm)	0.197	0.197	0.039	0.044	0.014	0.014	0.090	0.089	0.017	~ 7200
	0.005	0.003	0.001	0.001	0.000	0.000	0.003	0.003	0.001	
3 (L=4 mm, W=4 mm)	0.206	0.206	0.029	0.046	0.014	0.014	0.091	0.085	0.012	~ 10800
	0.001	0.002	0.002	0.001	0.001	0.001	0.002	0.007	0.002	

Table 3: The maximum values for the number of crossing per fiber n_{cpf}, and normalized effective elastic properties with Azimuthal orientation variation $\Delta\theta$. Here, μ and σ refer to the mean value and standard deviation, respectively. Here, volume fraction is set to be V_f≈0.28.

Set	max(n_{cpf})	$\frac{E_X}{E_x}$ (-) (μ, σ)	$\frac{E_Y}{E_x}$ (-) (μ, σ)	$\frac{E_Z}{E_x}$ (-) (μ, σ)	$\frac{G_{XY}}{E_x}$ (-) (μ, σ)	$\frac{G_{XZ}}{E_x}$ (-) (μ, σ)	$\frac{G_{YZ}}{E_x}$ (-) (μ, σ)	ν_{XY} (-) (μ, σ)	ν_{XZ} (-) (μ, σ)	ν_{YZ} (-) (μ, σ)
4 ($\Delta\theta$=±15°)	58	0.281 0.011	0.065 0.006	0.017 0.001	0.048 0.001	0.028 0.001	0.011 0.001	0.138 0.011	0.011 0.004	0.203 0.011
5 ($\Delta\theta$=±45°)	104	0.269 0.001	0.226 0.002	0.050 0.002	0.059 0.002	0.024 0.001	0.014 0.001	0.107 0.018	0.031 0.005	0.071 0.005
6 ($\Delta\theta$=±90°)	112	0.256 0.006	0.256 0.006	0.040 0.002	0.057 0.001	0.017 0.001	0.018 0.001	0.110 0.002	0.101 0.013	0.016 0.002

Table 4: The maximum values for the number of crossing per fiber n_{cpf}, and normalized effective elastic properties with the fiber volume fraction V_f. Here, μ and σ refer to the mean value and standard deviation, respectively. Azimuthal orientation variation is set as $\Delta\theta$=±90°.

Set	max(n_{cpf})	$\frac{E_X}{E_x}$ (-) (μ, σ)	$\frac{E_Y}{E_x}$ (-) (μ, σ)	$\frac{E_Z}{E_x}$ (-) (μ, σ)	$\frac{G_{XY}}{E_x}$ (-) (μ, σ)	$\frac{G_{XZ}}{E_x}$ (-) (μ, σ)	$\frac{G_{YZ}}{E_x}$ (-) (μ, σ)	ν_{XY} (-) (μ, σ)	ν_{XZ} (-) (μ, σ)	ν_{YZ} (-) (μ, σ)
7 (V_f≈0.18)	90	0.174 0.001	0.175 0.001	0.038 0.001	0.039 0.001	0.012 0.001	0.014 0.001	0.098 0.002	0.093 0.001	0.020 0.001
8 (V_f≈0.25)	108	0.241 0.002	0.241 0.003	0.023 0.003	0.050 0.001	0.016 0.001	0.016 0.001	0.115 0.006	0.221 0.059	0.020 0.002
9 (V_f≈0.27)	112	0.256 0.006	0.256 0.006	0.040 0.002	0.057 0.001	0.017 0.001	0.018 0.001	0.110 0.002	0.101 0.013	0.016 0.002
10 (V_f≈0.30)	124	0.285 0.006	0.284 0.006	0.023 0.002	0.062 0.001	0.020 0.001	0.020 0.001	0.124 0.003	0.137 0.032	0.011 0.002

List of Figures

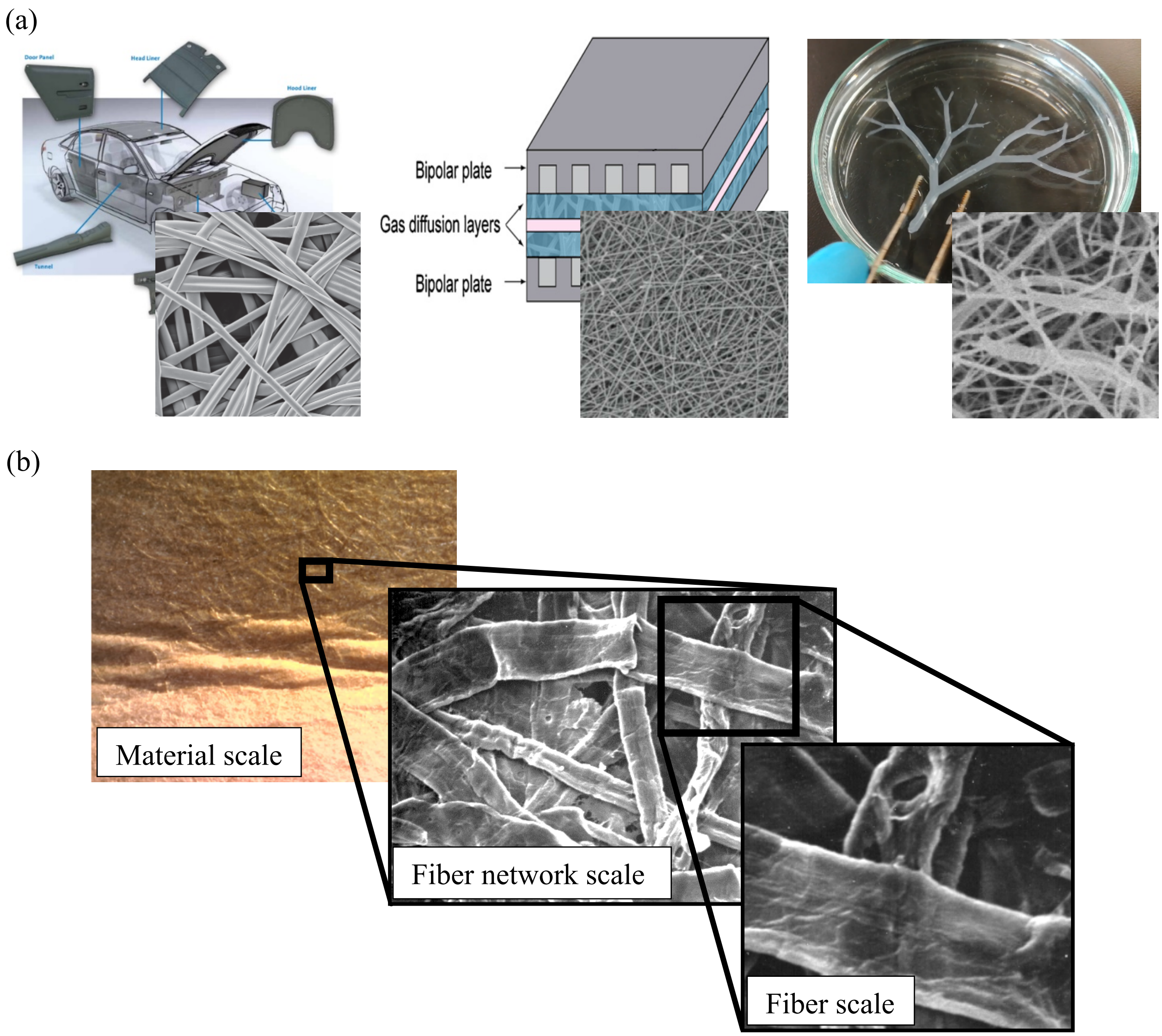

Figure 1: Fibrous materials and their heterogeneous nature: (a) various engineering applications, nonwoven car panel, fiber mat for gas diffusion layers and bacterial nanocellulose scaffold, and their microscope images, (b) material, fiber network and fiber scales definition for kraft paper.

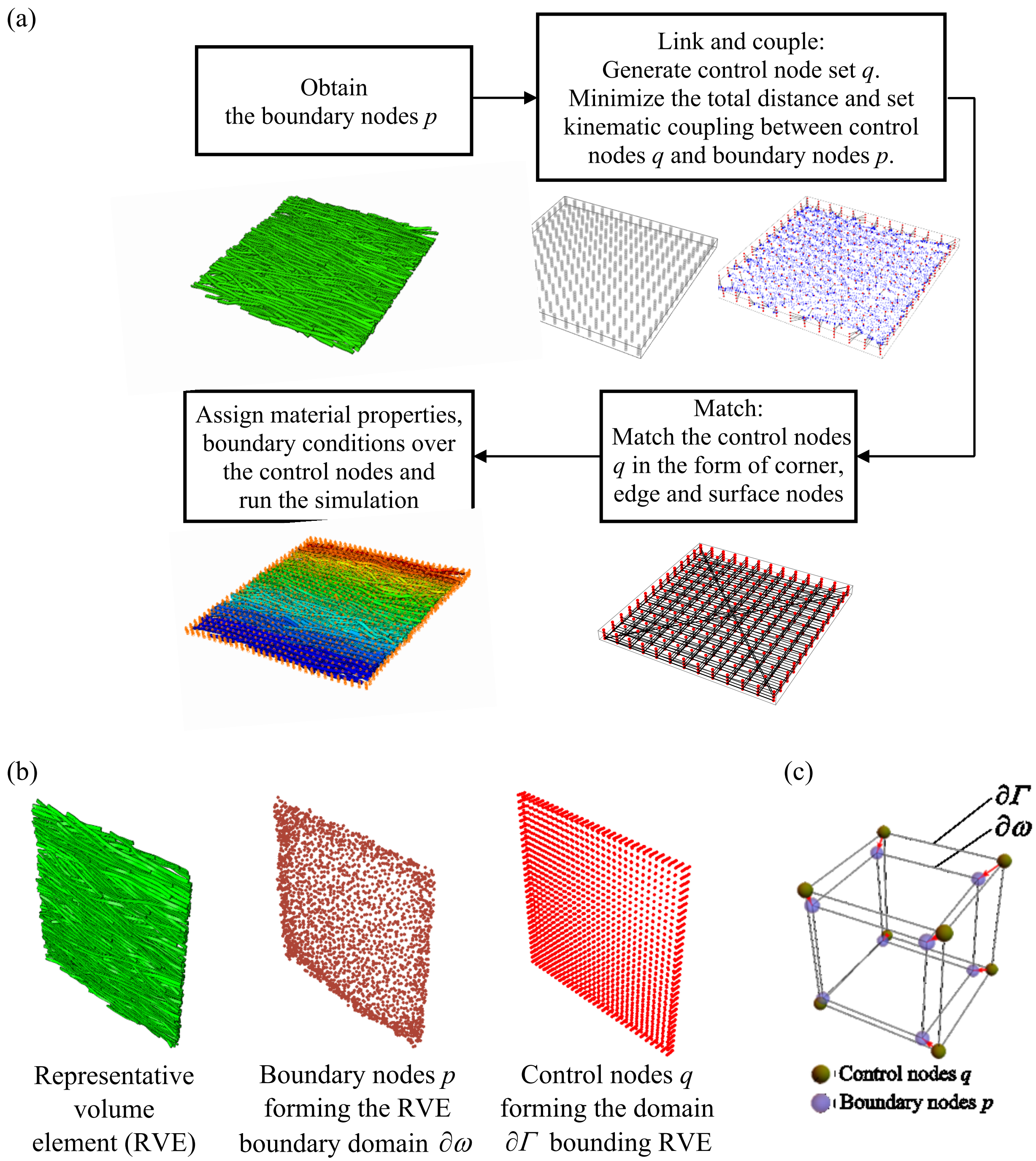

Figure 2. The schematic illustration of the present framework: (a) flow chart for the computational homogenization framework, (b) representative volume element (RVE) boundary domain represented with $\partial\omega$, domain $\partial\Gamma$ bounding RVE, boundary nodes p on $\partial\omega$ and control nodes q comprising of vertices, edge and surface nodes on $\partial\Gamma$, (c) elaboration of linking and kinematic coupling phenomenon between control and boundary nodes.

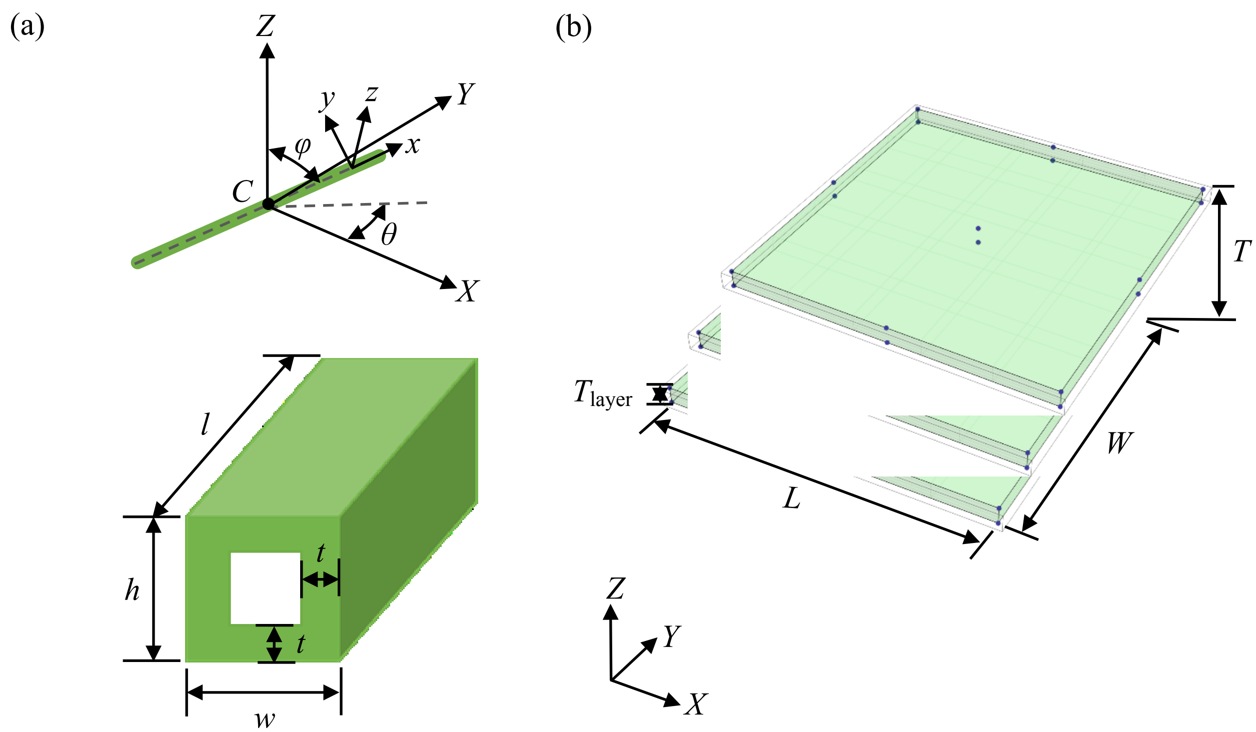

Figure 3. Fiber profile and distribution: (a) fiber spatial properties in global (specimen) *XYZ*-Cartesian coordinate system and geometrical properties in local (fiber) *xyz*-Cartesian coordinate system, (b) layered structure of specimen in global *XYZ*-Cartesian coordinate system.

(a)

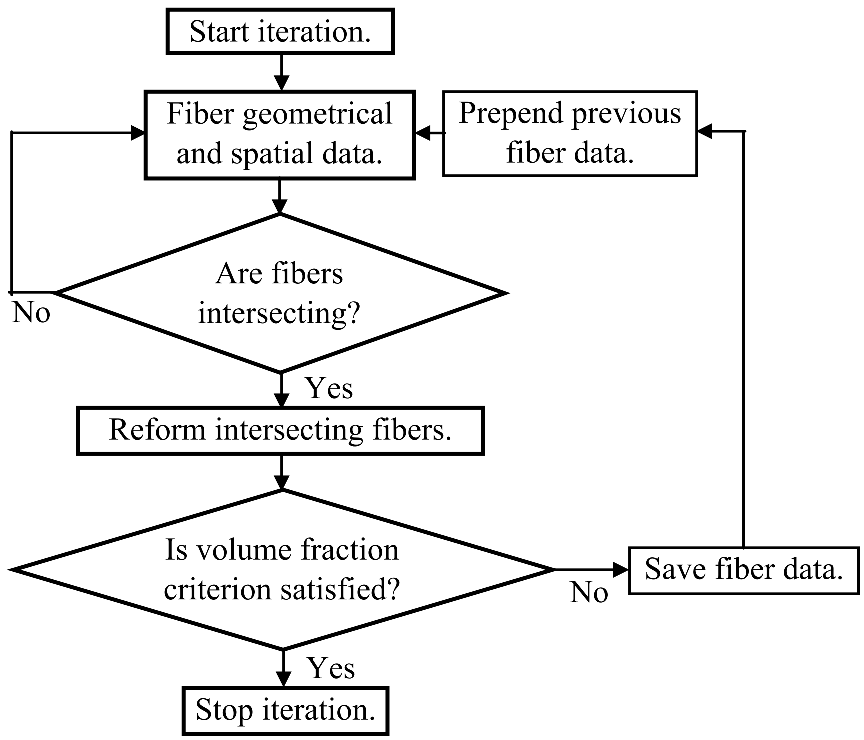

(b)

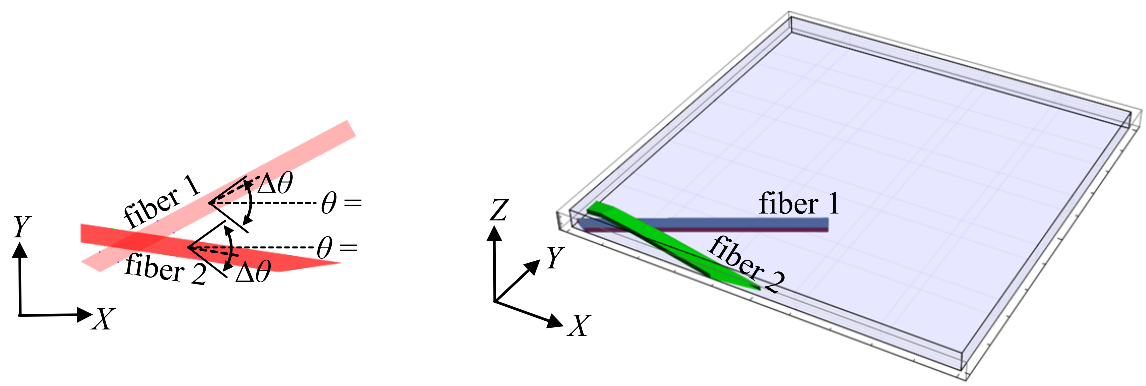

Figure 4. Fiber deposition process: (a) flow chart of the algorithm; (b) schematic illustration of the fiber orientations during the deposition.

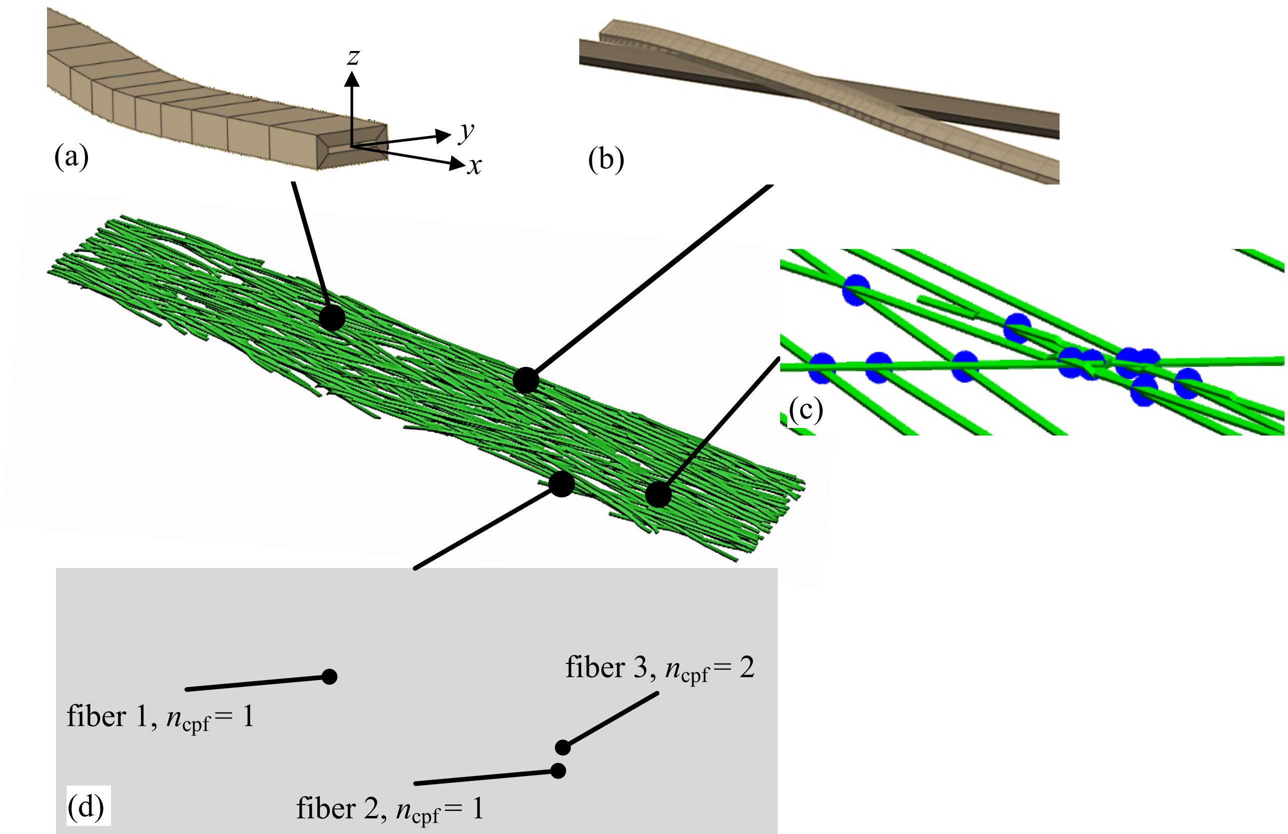

Figure 5. Schematic representation of fiber network representing individual fibers with (a) material direction definitions, (b) intersecting fibers, (c) contact regions and (d) concept of number of crossings per fiber n_{cpf}. Here, blue dots represent the crossings.

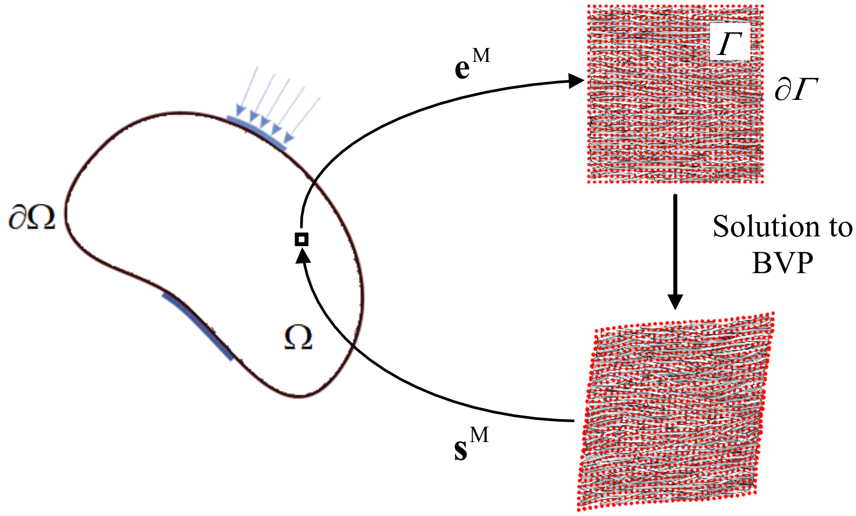

Figure 6. Strain driven homogenization with imposed macroscopic strain $\mathbf{e}^{\mathrm{M}}$ and computed stress $\mathbf{s}^{\mathrm{M}}$. Here, Ω and $\partial\Omega$ represent the volume and boundary of continuum, and Γ and $\partial\Gamma$ represent the volume and boundary of the domain (in the form of rectangular prism) bounding the RVE.

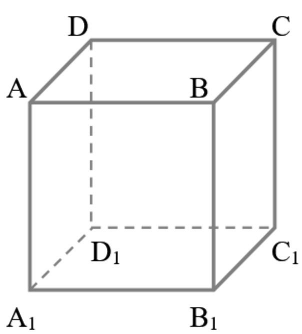

Corner nodes	Edge nodes	Surface nodes
Node at point A □	Nodes on edge AB ●	Nodes on surface ABCD ♦
Node at point B □	Nodes on edge BC ○	Nodes on surface $A_1B_1C_1D_1$ ♦
Node at point C □	Nodes on edge DC ●	Nodes on surface AA_1D_1D ◘
Node at point D □	Nodes on edge AD ○	Nodes on surface BB_1C_1C ◘
Node at point A_1 □	Nodes on edge A_1B_1 ●	Nodes on surface DD_1C_1C ⌂
Node at point B_1 □	Nodes on edge B_1C_1 ○	Nodes on surface AA_1B_1B ⌂
Node at point C_1 □	Nodes on edge D_1 C_1 ●	
Node at point D_1 □	Nodes on edge A_1 D_1 ○	
	Nodes on edge A_1A ◊	
	Nodes on edge B_1B ◊	
	Nodes on edge C_1C ◊	
	Nodes on edge D_1D ◊	

Figure 7. Illustration of control node sets q on $\partial\Gamma$ used in the periodic boundary condition equations for an RVE. The symbols on the right-hand sides of the nodes show the matching sets for the periodicity.

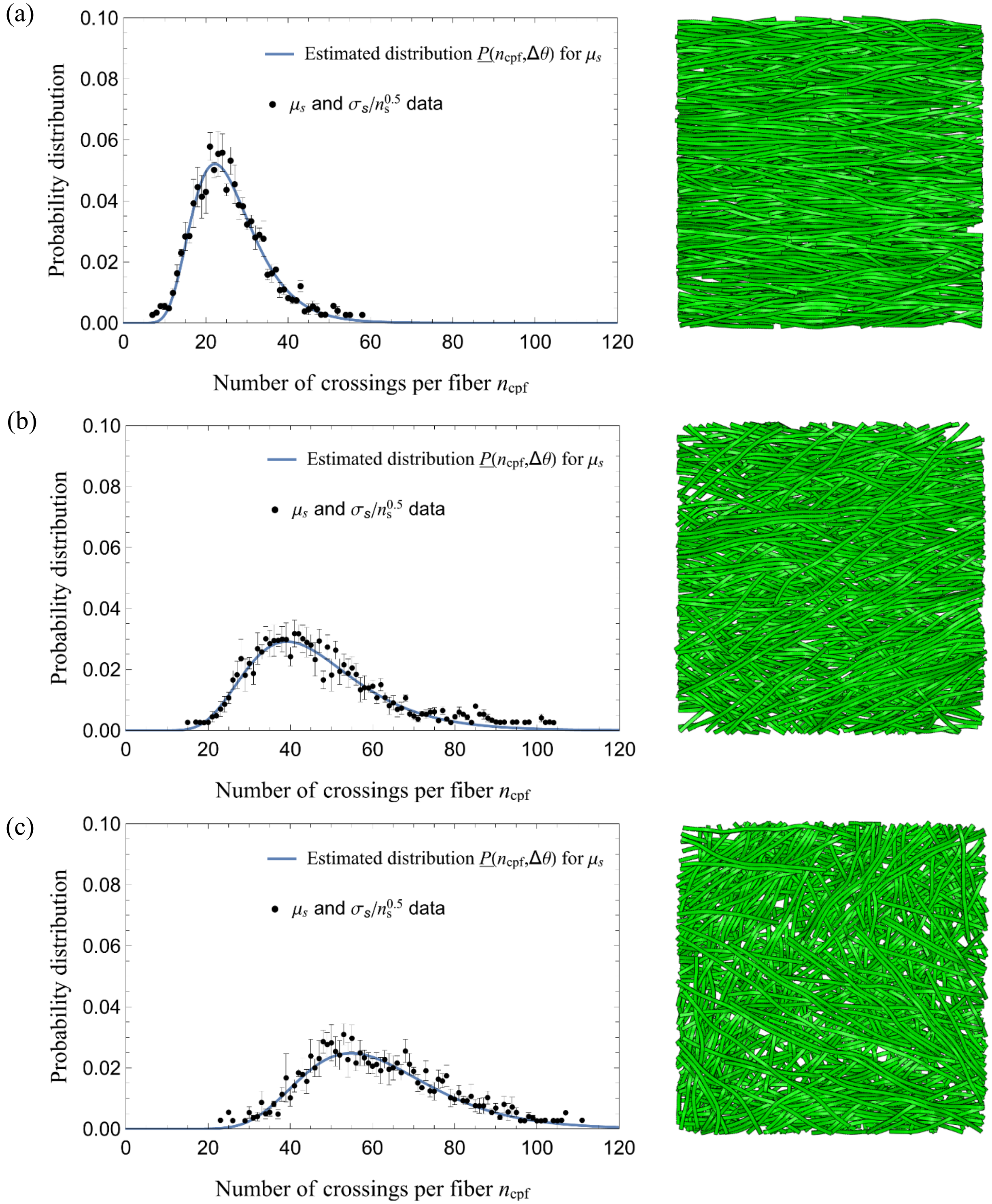

Figure 8: Representation of fiber orientation variation $\Delta\theta$ effect on the number of crossing per fiber n_{cpf} as continuous probability distribution: (a) $\Delta\theta$=±15°, (b) $\Delta\theta$=±45°, (c) $\Delta\theta$=±90°. Depicted solution domains show the fiber alignment based on the designated $\Delta\theta$ where V_f≈0.28.

(a)

(b)

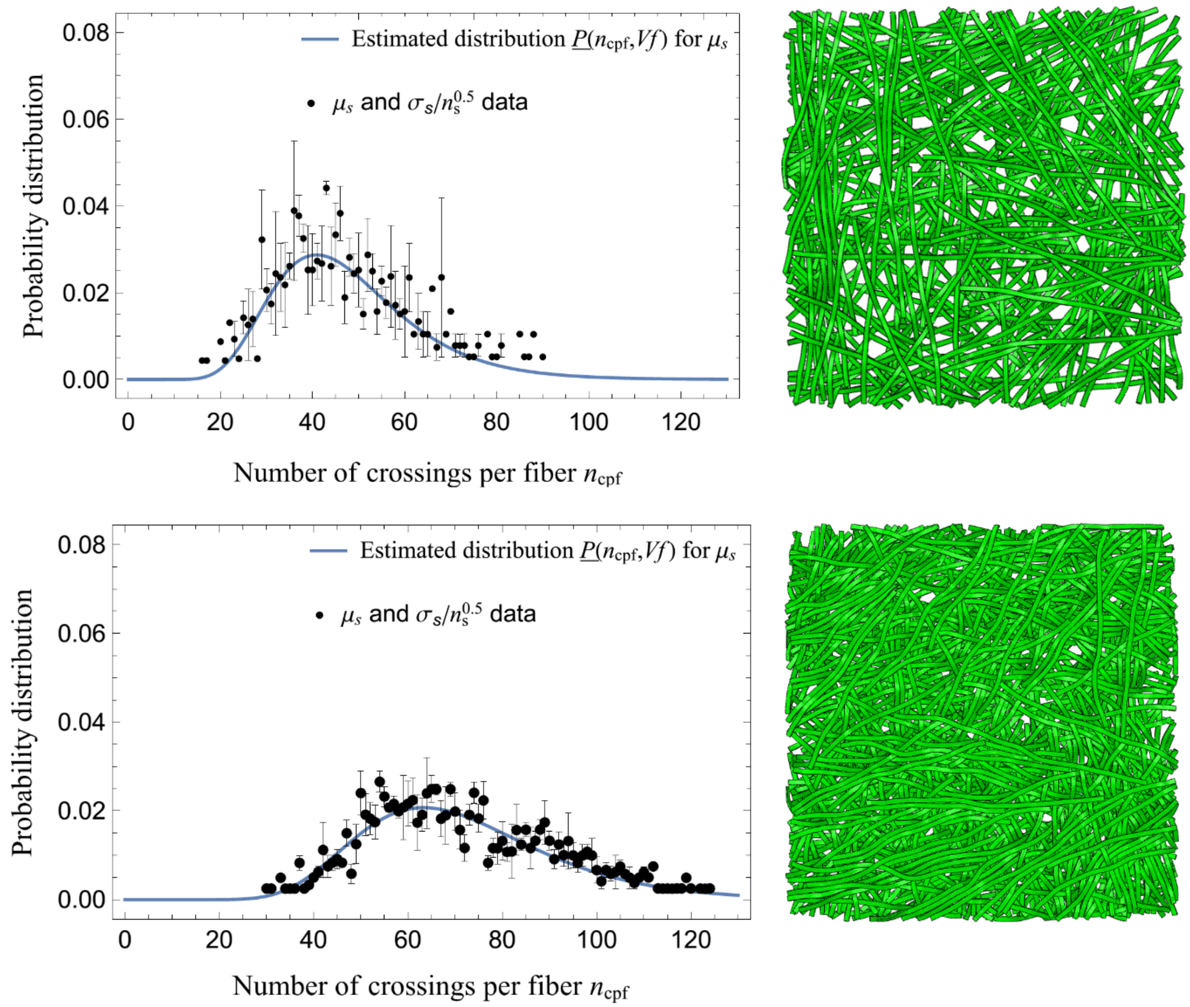

Figure 9: Effect of fiber volume fraction V_f on the number of crossing per fiber (a) $V_f \approx 18\%$, (b) $V_f \approx 30\%$. Here, Azimuthal orientation variation was set as $\Delta\theta = \pm 90°$.

The authors declare no conflict of interest.

All authors have read and agree to the published version of the manuscript. Conceptualization, A.K.; methodology, A.K.; formal analysis, A.K.; investigation, A.K.; writing—original draft preparation, A.K., E.T.; writing—review and editing, A.K., E.T. J.P.; visualization, A.K.; funding acquisition, J.P..